Science Advances
AAAS

Supplementary Materials for

Construction of solid-liquid fluorine transport channel to enable highly reversible conversion cathodes

Keyi Chen, Meng Lei, Zhenguo Yao, Yongjian Zheng, Jiulin Hu, Chuanzhong Lai, Chilin Li*

*Corresponding author. Email: chilinli@mail.sic.ac.cn

Published 3 November 2021, *Sci. Adv.* **7**, eabj1491 (2021)
DOI: 10.1126/sciadv.abj1491

This PDF file includes:

Supporting Information for

Construction of Solid-Liquid Fluorine-Transport Channel to Enable Highly Reversible Conversion Cathodes

Keyi Chen [1,2,3], *Meng Lei* [1,3], *Zhenguo Yao* [1,2], *Yongjian Zheng* [1,2,3], *Jiulin Hu* [1,2,3], *Chuanzhong Lai* [1,2,3] *and Chilin Li* [1,2,3]*

[1] State Key Laboratory of High Performance Ceramics and Superfine Microstructure, Shanghai Institute of Ceramics, Chinese Academy of Sciences, 585 He Shuo Road, Shanghai 201899, China. Email: chilinli@mail.sic.ac.cn

[2] Center of Materials Science and Optoelectronics Engineering, University of Chinese Academy of Sciences, Beijing 100049, China.

[3] CAS Key Laboratory of Materials for Energy Conversion, Shanghai Institute of Ceramics, Chinese Academy of Sciences, Shanghai 201899, China.

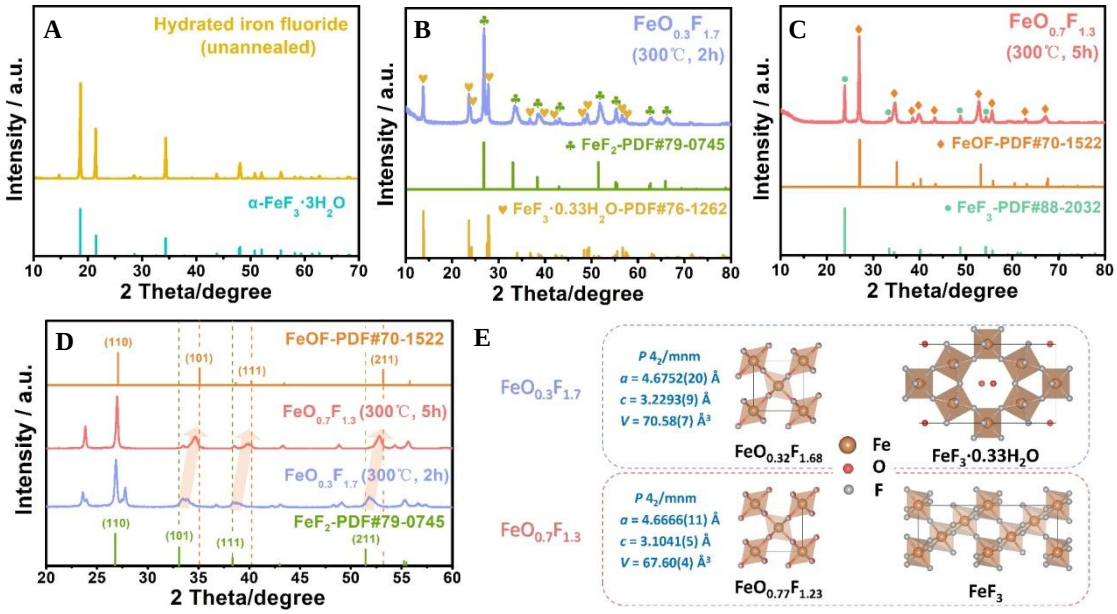

Figure S1. XRD characterization of as-prepared iron (oxy)fluorides and hydrated iron fluoride precursor. XRD patterns of (**A**) hydrated iron fluoride precursor, (**B**) $FeO_{0.3}F_{1.7}$, and (**C**) $FeO_{0.7}F_{1.3}$. The pattern of hydrated precursor can be well indexed to α-$FeF_3 \cdot 3H_2O$ based on the corresponding

reference diffractogram. (**D**) Magnified XRD patterns of as-prepared iron oxyfluorides in a 2θ range of 20°-60° with the tagged shift in correlative diffraction peaks in comparison with the standard diffractograms of rutile-type FeF_2 and FeOF. (**E**) Crystal structures of dominant FeO_xF_{2-x} phases and minor phases of trigonal FeF_3 and HTB-type $FeF_3 \cdot 0.33H_2O$. The calculated lattice parameters for dominant phases are noted. In crystallographic structures of FeO_xF_{2-x}, the octahedral site surrounding central Fe atom is shown in a ball with two colors, denoting the probability of site occupation by O atom or F atom.

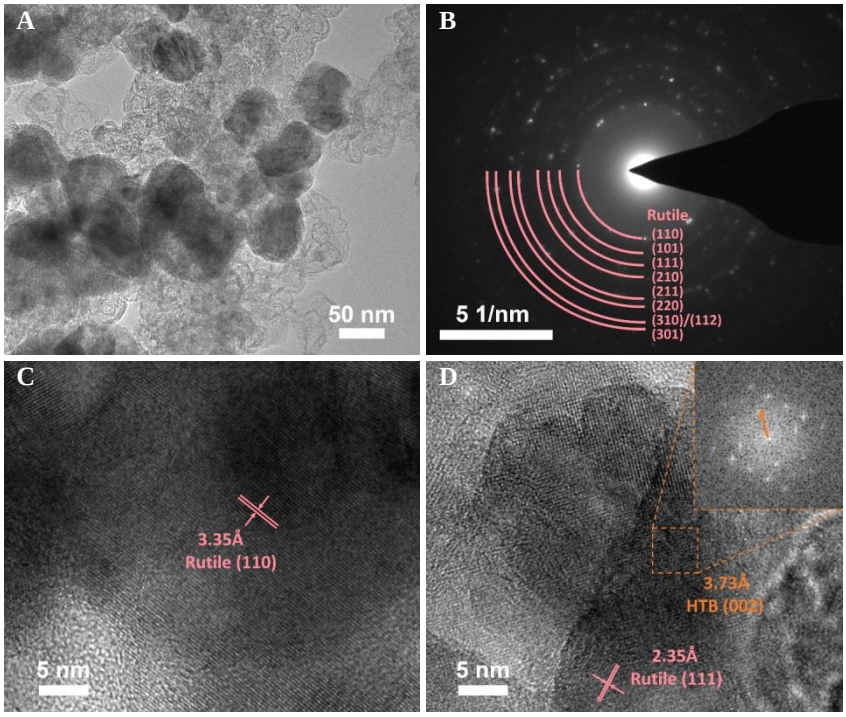

Figure S2. TEM measurement of $FeO_{0.3}F_{1.7}$. (**A**) TEM image of $FeO_{0.3}F_{1.7}$ and (**B**) corresponding SAED pattern. (**C,D**) HRTEM images in different magnified regions, clear showing the lattice strips corresponding to dominant rutile $FeO_{0.32}F_{1.68}$ and minor hexagonal $FeF_3 \cdot 0.33H_2O$. Inset of (**D**): FFT pattern at selected region with the marked diffraction spots assigned to (002) plane of HTB-type fluoride.

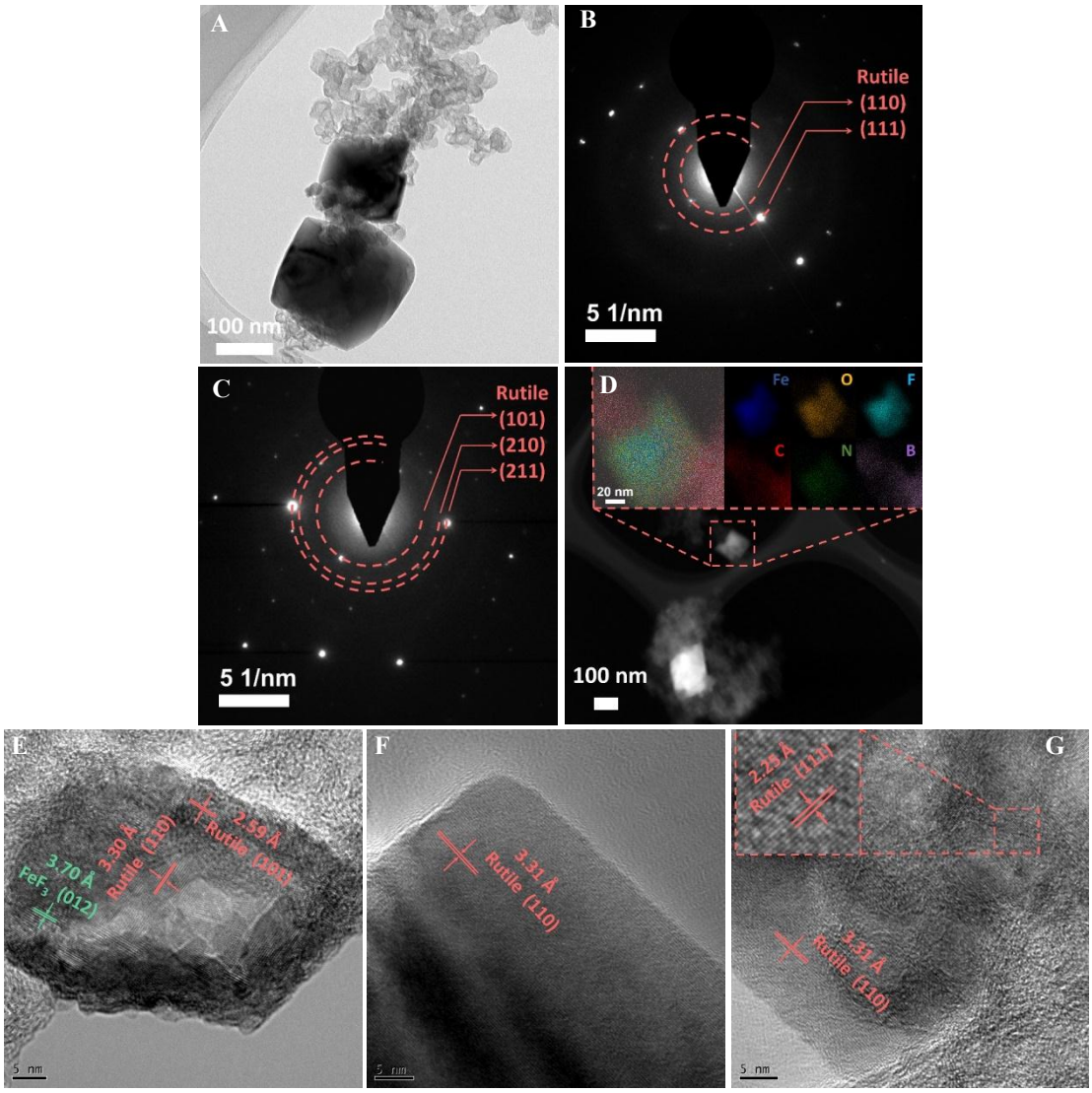

Figure S3. TEM measurement of $FeO_{0.7}F_{1.3}$ (**A**) TEM image of $FeO_{0.7}F_{1.3}$ and (**B,C**) corresponding SAED patterns. (**D**) HAADF image of $FeO_{0.7}F_{1.3}$. Inset of (**D**): HAADF-STEM mapping of selected region with octahedral fluoride and surrounding KB/IL (containing Fe, O, F, C, N, and B elements). (**E-G**) HRTEM images in different magnified regions, clear showing the lattice strips corresponding to dominant rutile $FeO_{0.77}F_{1.23}$ and minor trigonal FeF_3.

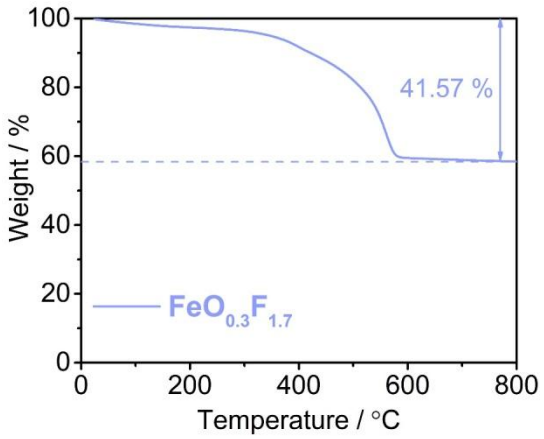

Figure S4. TGA curve of $FeO_{0.3}F_{1.7}$ with the weight loss under an O_2 flow from room temperature to 800 °C.

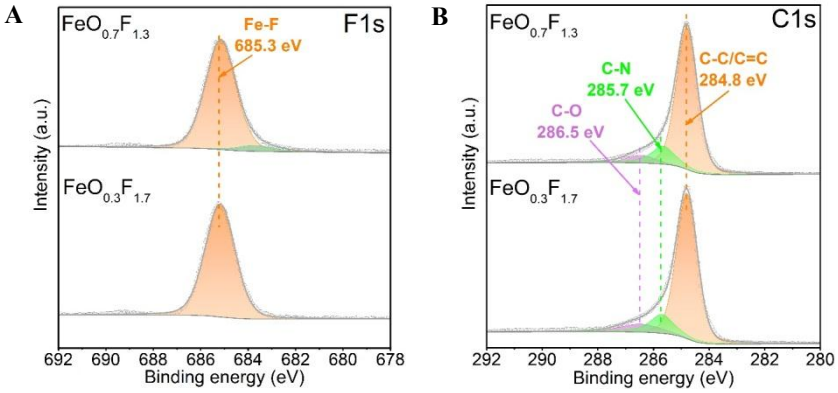

Figure S5. XPS spectra of (**A**) F 1s and (**B**) C 1s for $FeO_{0.3}F_{1.7}$ and $FeO_{0.7}F_{1.3}$.

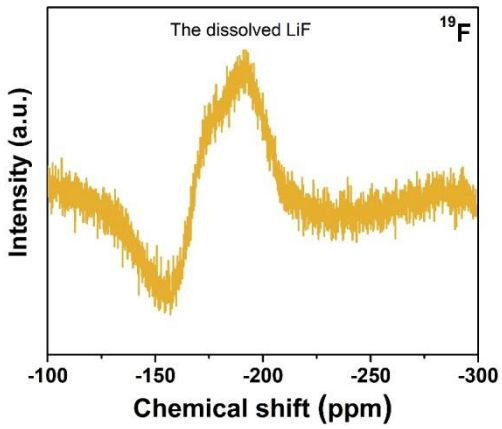

Figure S6. ^{19}F NMR spectrum of the dissolved LiF in dimethyl sulfoxide.

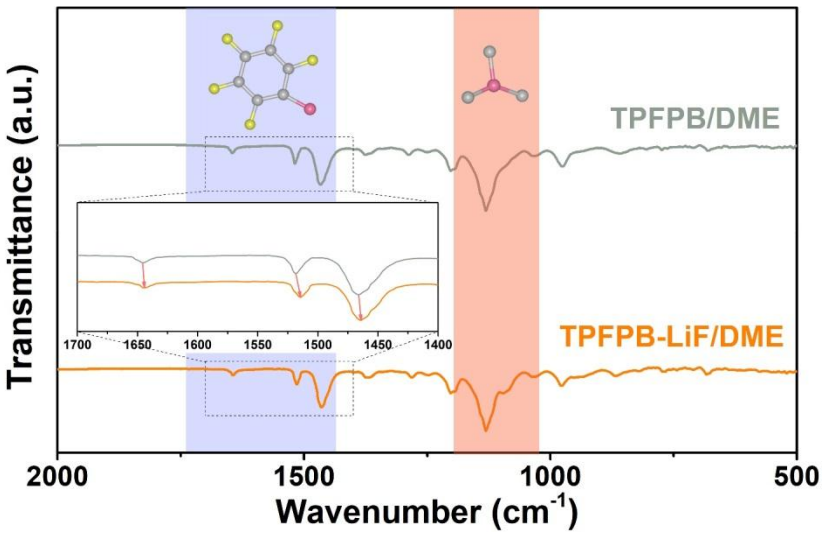

Figure S7. FTIR spectra of TPFPB/DME and TPFPB-LiF/DME solutions, inset: magnified FTIR spectra in the range of 1400-1700 cm^{-1}.

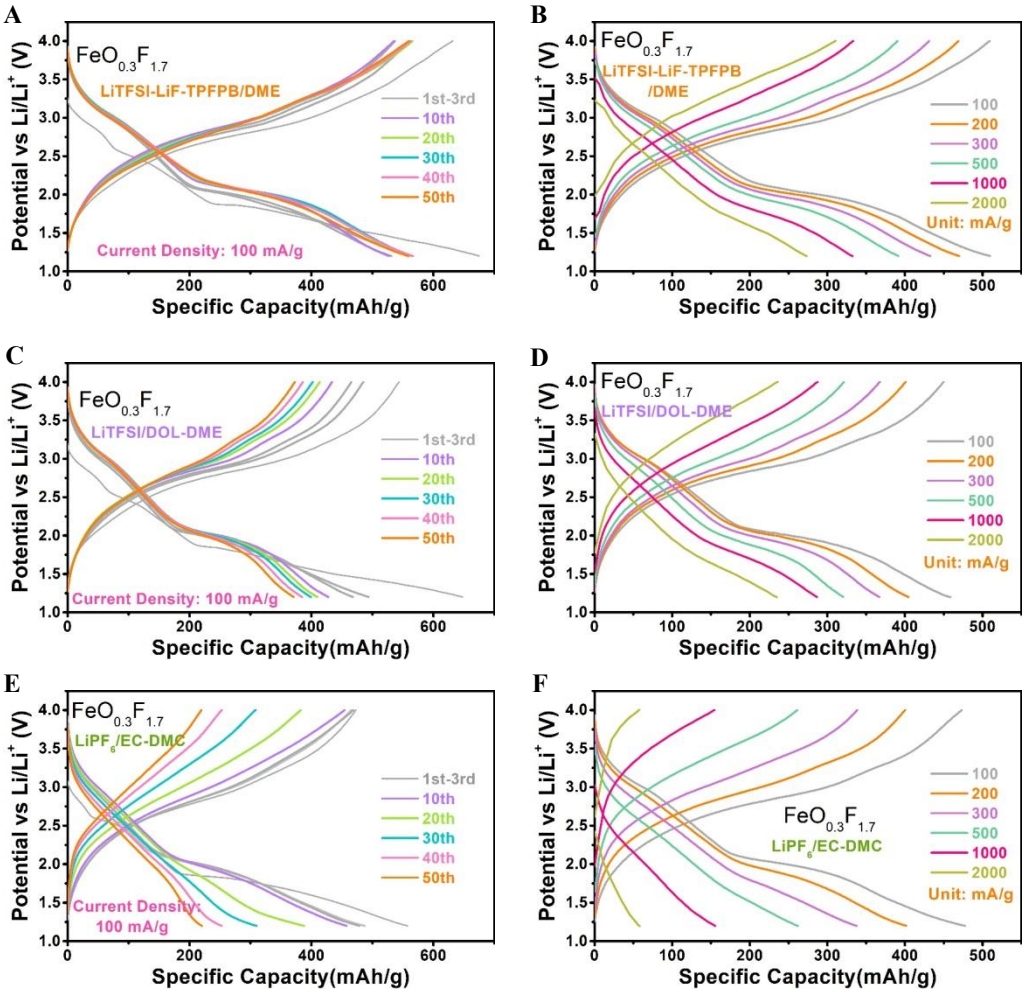

Figure S8. Li-storage performance of $FeO_{0.3}F_{1.7}$ cathode in different electrolytes. Charge-discharge curves of Li/$FeO_{0.3}F_{1.7}$ cells under a current density of 100 mA/g in the systems of (**A**) TPFPB-containing ether electrolyte (LiTFSI-LiF-TPFPB/DME), (**C**) ether-based electrolyte (LiTFSI/DOL-DME) and (**E**) carbonate-based electrolyte ($LiPF_6$/EC-DMC) at different cycling stages. Rate performance of $FeO_{0.3}F_{1.7}$ cathodes at various current densities from 100 to 2000 mA/g in different electrolyte systems of (**B**) LiTFSI-LiF-TPFPB/DME, (**D**) LiTFSI/DOL-DME and (**F**) $LiPF_6$/EC-DMC.

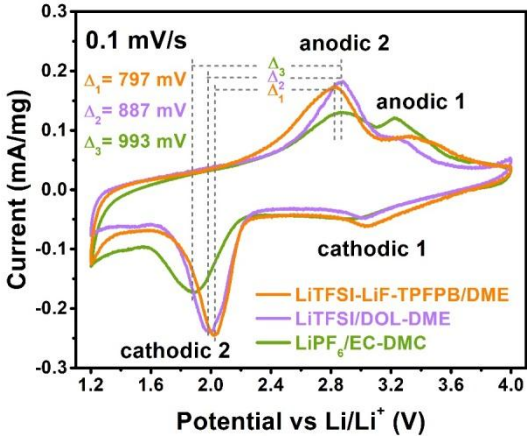

Figure S9. Typical CV curves of Li/$FeO_{0.3}F_{1.7}$ cells based on different electrolytes at a scan rate of 0.1 mV/s.

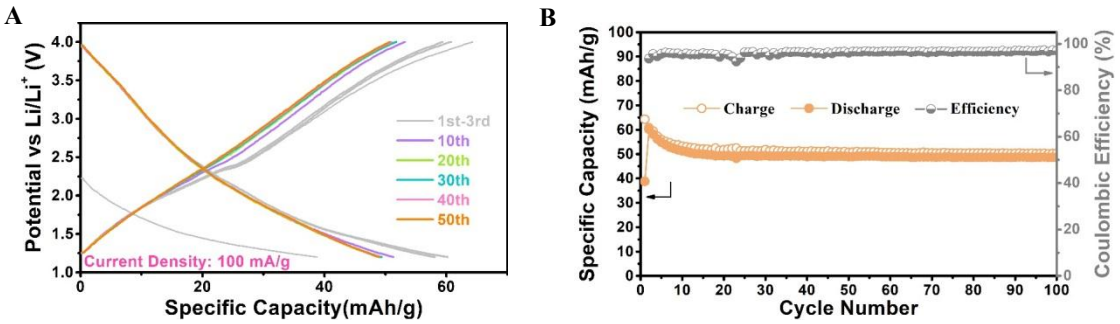

Figure S10. Li-storage performance of KB-only control cathode. (**A**) Charge-discharge curves and (**B**) cycling performance and coulombic efficiency of KB-only control cathode using LiTFSI/DOL-DME electrolyte at a current density of 100 mA/g.

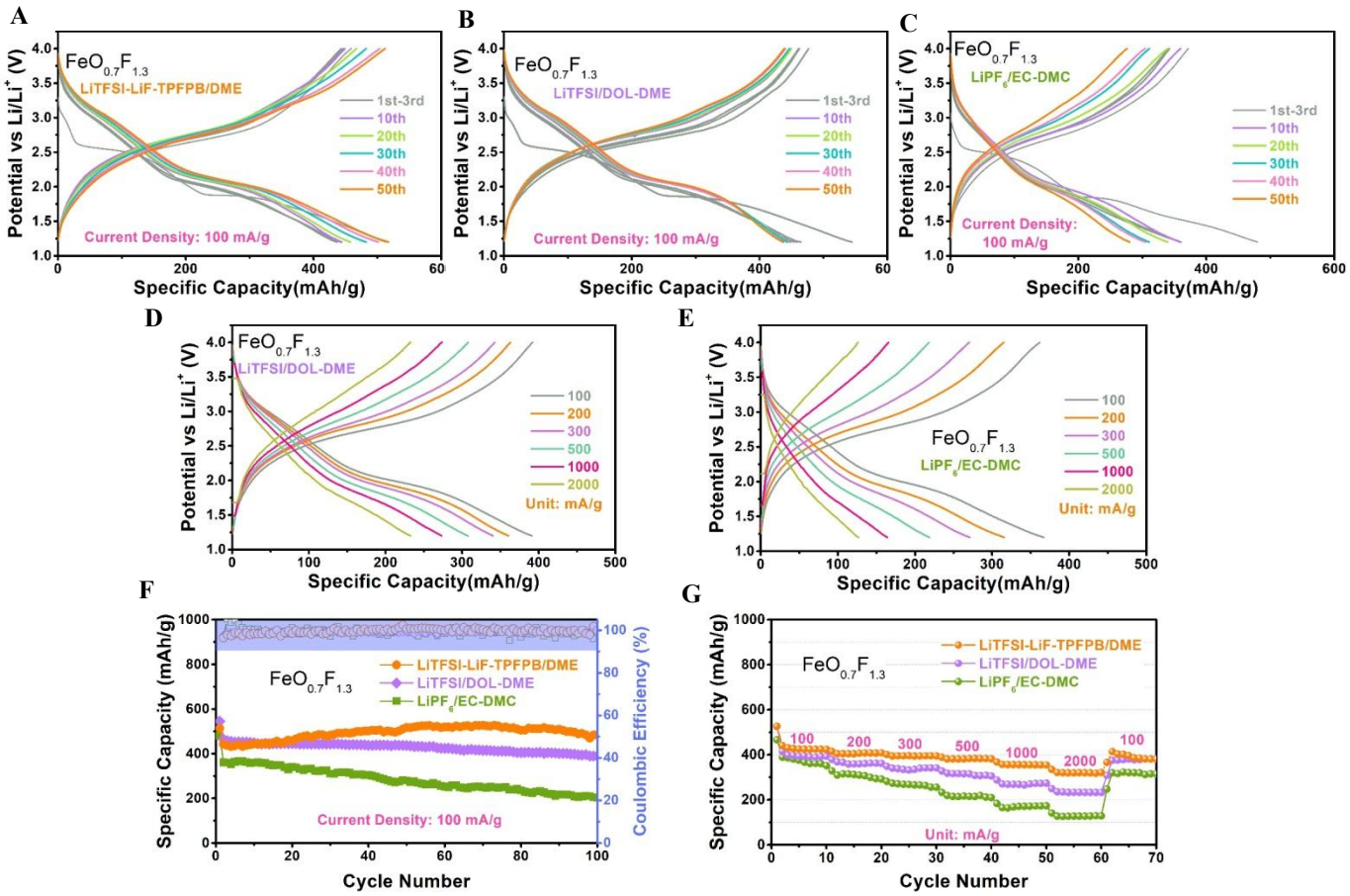

Figure S11. Li-storage performance of $FeO_{0.7}F_{1.3}$ cathode in different electrolytes. Galvanostatic charge-discharge curves of $FeO_{0.7}F_{1.3}$ cathodes with the electrolytes of (**A**) LiTFSI-LiF-TPFPB/DME, (**B**) LiTFSI/DOL-DME and (**C**) $LiPF_6$/EC-DMC at a current density of 100 mA/g in different cycling stages. Typical charge-discharge profiles of $FeO_{0.7}F_{1.3}$ cathodes at various current densities when using the electrolytes of (**D**) LiTFSI/DOL-DME and (**E**) $LiPF_6$/EC-DMC without TPFPB additive. Comparison of (**F**) cycling capability and (**G**) rate performance of $FeO_{0.7}F_{1.3}$ cathodes with LiTFSI-LiF-TPFPB/DME electrolyte and the control ether- and carbonate- based electrolytes.

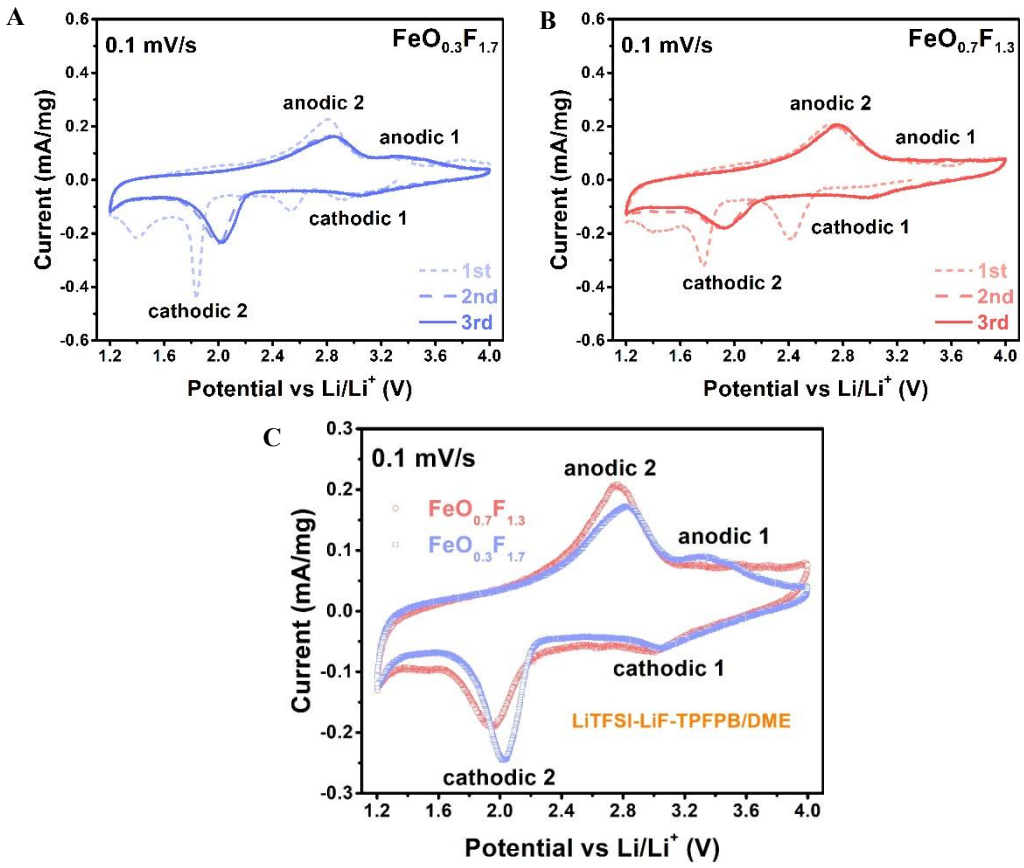

Figure S12. CV measurement for oxyfluoride cathodes in LiTFSI-LiF-TPFPB/DME electrolyte at a scan rate of 0.1 mV/s in the voltage range of 1.2–4.0 V. CV profiles of (**A**) Li/$FeO_{0.3}F_{1.7}$ and (**B**) Li/$FeO_{0.7}F_{1.3}$ cells during the first three cycles. (**C**) Comparison of reversible CV curves of $FeO_{0.7}F_{1.3}$ and $FeO_{0.3}F_{1.7}$ cathodes.

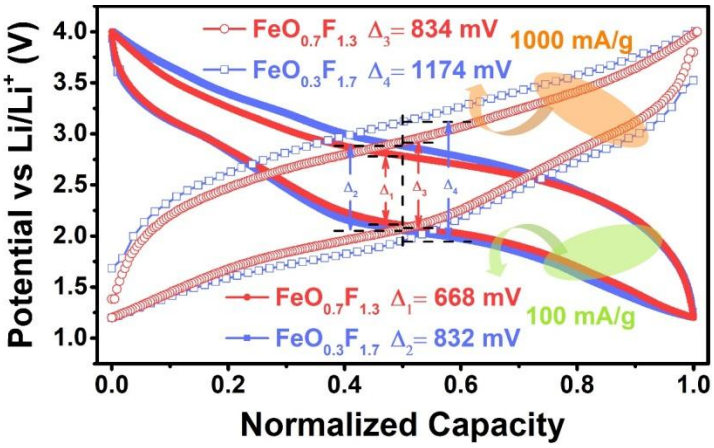

Figure S13. Potential versus normalized capacity profiles of $FeO_{0.7}F_{1.3}$ and $FeO_{0.3}F_{1.7}$ in LiTFSI-LiF-TPFPB/DME electrolyte at 100 mA/g and 1000 mAh/g, respectively. Labeled overpotential values are obtained from voltage difference between charge and discharge at the middle position of normalized capacity.

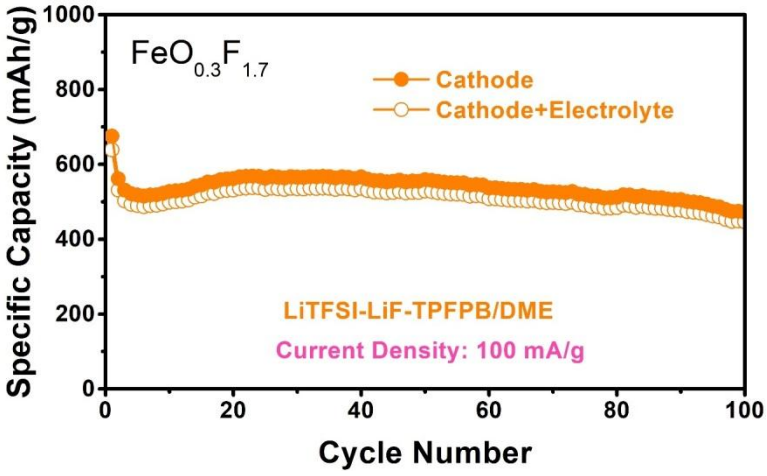

Figure S14. Discharge capacities of $Li/FeO_{0.3}F_{1.7}$ cells with LiTFSI-LiF-TPFPB/DME electrolyte, which are estimated based on the only weight of $FeO_{0.3}F_{1.7}$ in cathode and based on the weights of $FeO_{0.3}F_{1.7}$ and dissolved LiF in electrolyte.

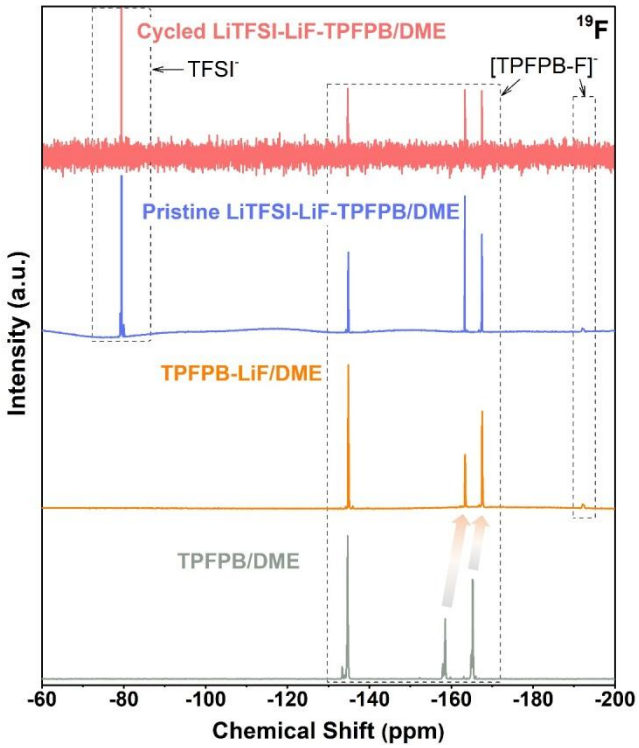

Figure S15. ^{19}F NMR spectra of pristine and cycled LiTFSI-LiF-TPFPB/DME electrolyte, as well as their comparison with TPFPB-LiF/DME and TPFPB/DME solutions.

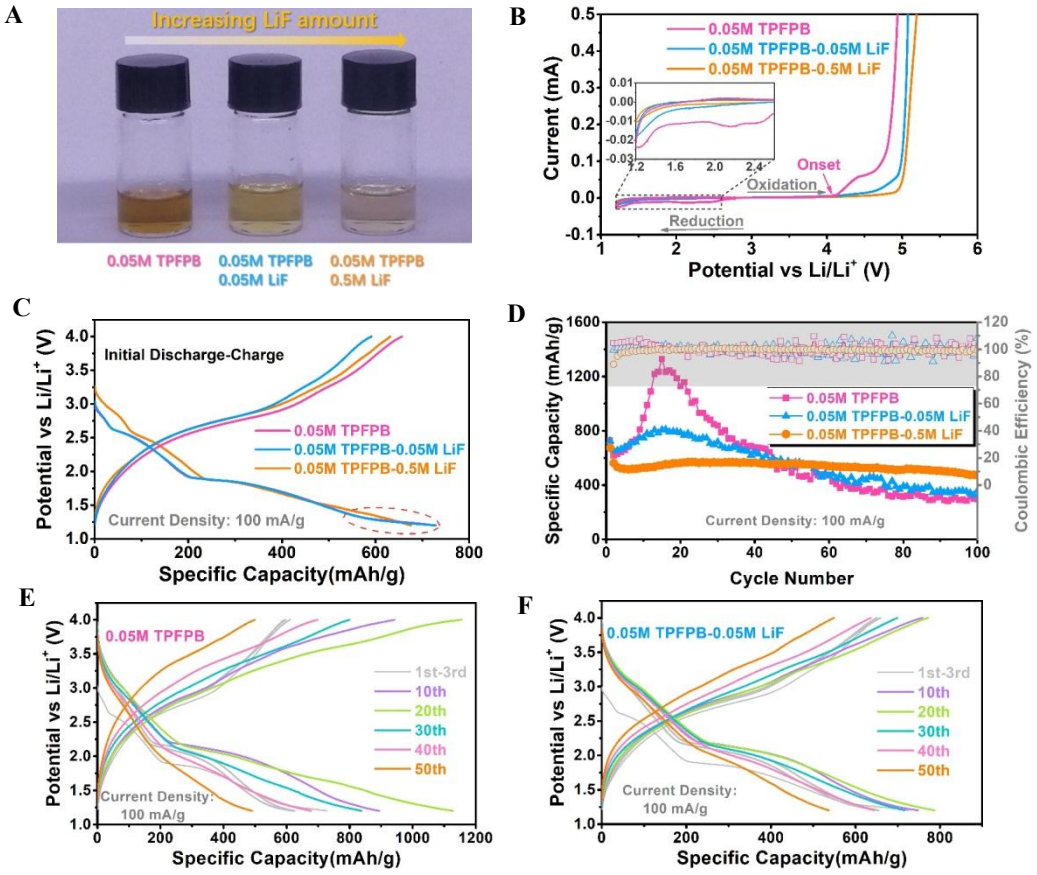

Figure S16. Optimization of TPFPB-containing electrolytes based on electrochemical stability window measurement and Li-storage performance of $FeO_{0.3}F_{1.7}$. (**A**) Optical images of LiTFSI-DME electrolytes with 0.05 M TPFPB and different amount of LiF. (**B**) Typical CV curves of different TPFPB-containing electrolytes at a scan rate of 2 mV/s measured in coin cells with Al and Li foil as the working and counter electrodes, inset of (**B**): Magnified CV plots between 1.2 and 2.5 V. Comparison of (**C**) initial discharge-charge curves and (**D**) cycling performance of $FeO_{0.3}F_{1.7}$ cathode using various TPFPB-containing electrolytes at a current density of 100 mA/g. Galvanostatic charge-discharge curves of $FeO_{0.3}F_{1.7}$ cathode in the cases of (**E**) 0.05 M TPFPB and (**F**) 0.05M TPFPB-0.05M LiF electrolytes at different cycling stages. Photo Credit: Keyi Chen, Shanghai Institute of Ceramics, Chinese Academy of Sciences.

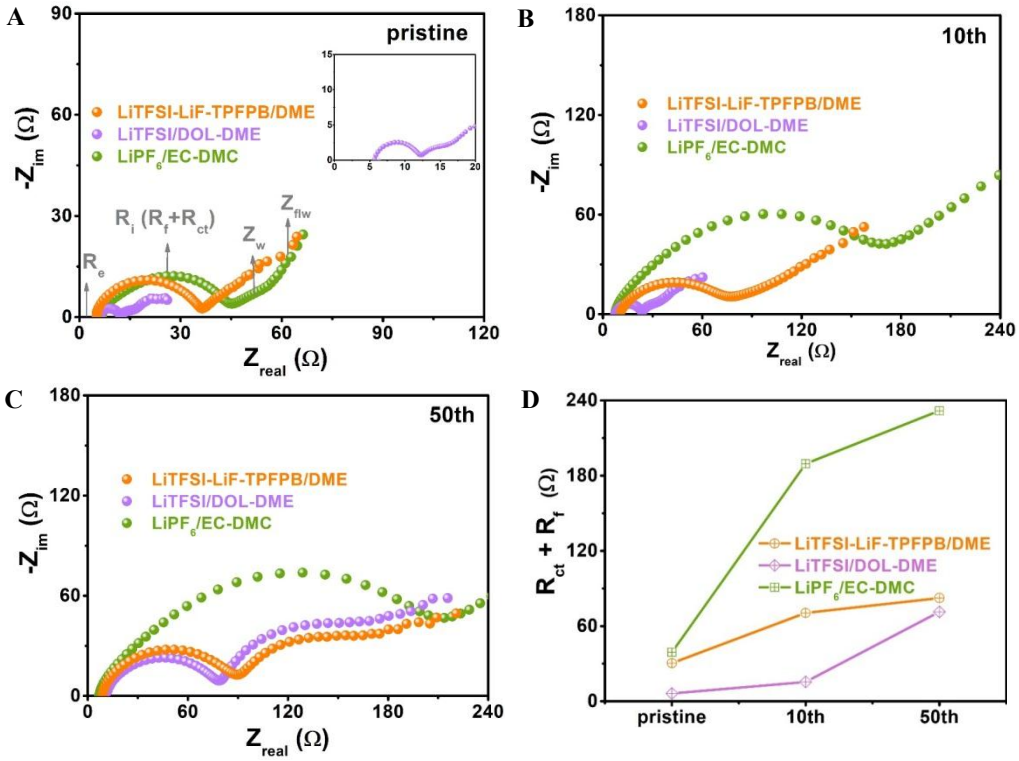

Figure S17. Electrochemical impedance spectra evolution of Li/$FeO_{0.3}F_{1.7}$ cells with different electrolytes. Nyquist plots of Li/$FeO_{0.3}F_{1.7}$ cells with the electrolytes of LiTFSI-LiF-TPFPB/DME, LiTFSI/DOL-DME and $LiPF_6$/EC-DMC (**A**) in pristine state, (**B**) after 10 cycles and after (**C**) 50 cycles at 100 mA/g. (**D**) Evolution of interface resistance R_i values (obtained from the fitted near-completed semicircle in high frequencies, contributed by both CEI/SEI film resistance R_f and charge transfer resistance R_{ct}) for the three cells with different electrolytes at different cycling stages.

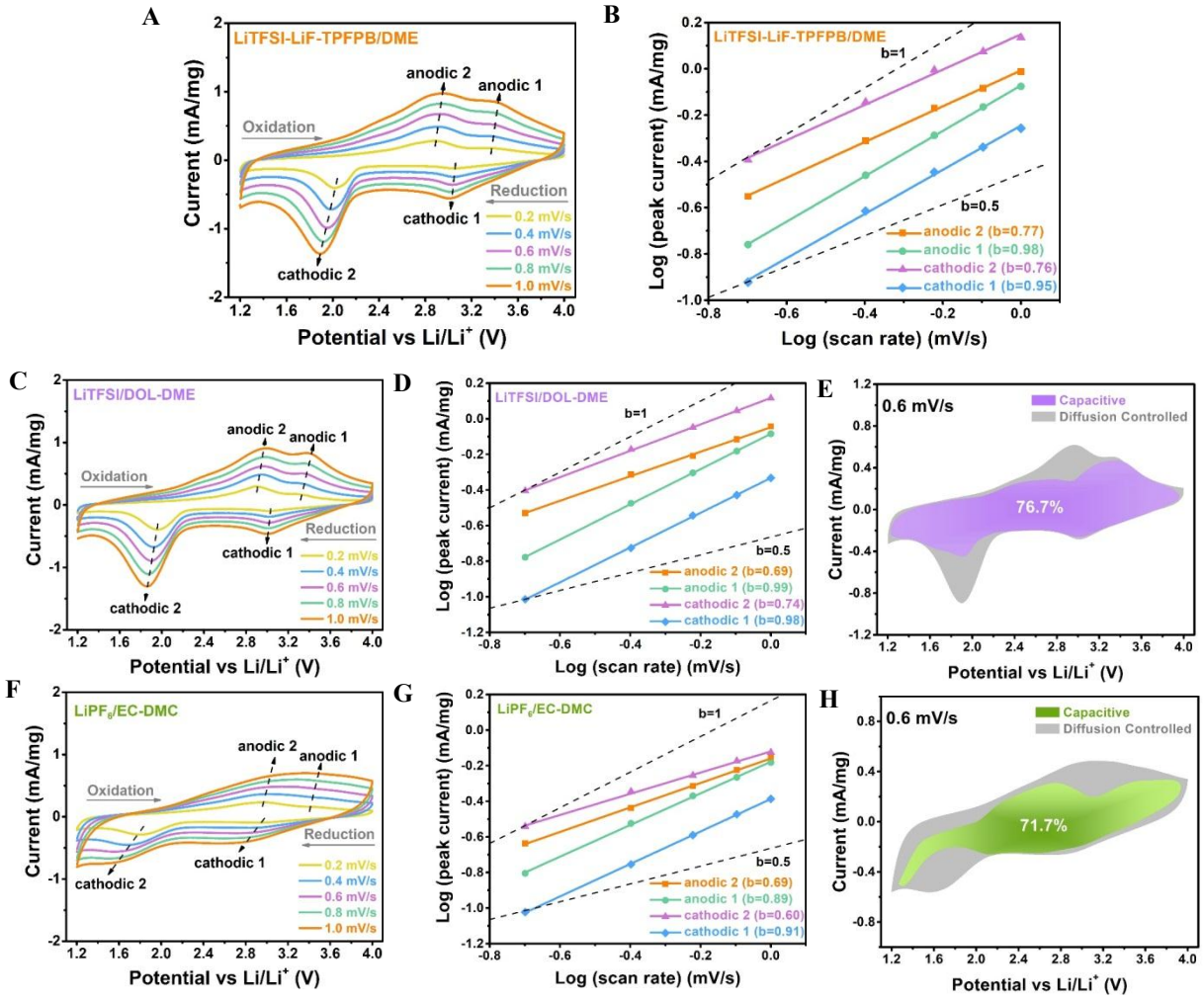

Figure S18. Charge-storage mechanism analysis of $FeO_{0.3}F_{1.7}$ cathode in different electrolytes. Typical CV curves of $FeO_{0.3}F_{1.7}$ cathode at various scan rates from 0.2 to 1.0 mV/s when cycled in (**A**) LiTFSI-LiF-TPFPB/DME, (**C**) LiTFSI/DOL-DME and (**F**) $LiPF_6$/EC-DMC electrolytes between 1.2 and 4.0 V with the characteristic peaks labeled. (**B**), (**D**) and (**G**) Power law dependence of measured current on scan rate at corresponding peak potentials based on log i(V) = b log v + log a in corresponding electrolyte systems. Typical CV curves of Li/$FeO_{0.3}F_{1.7}$ cells at 0.6 mV/s with divisional capacitive contribution and diffusion-controlled contribution using the electrolytes of (**E**) LiTFSI/DOL-DME and (**H**) $LiPF_6$/EC-DMC.

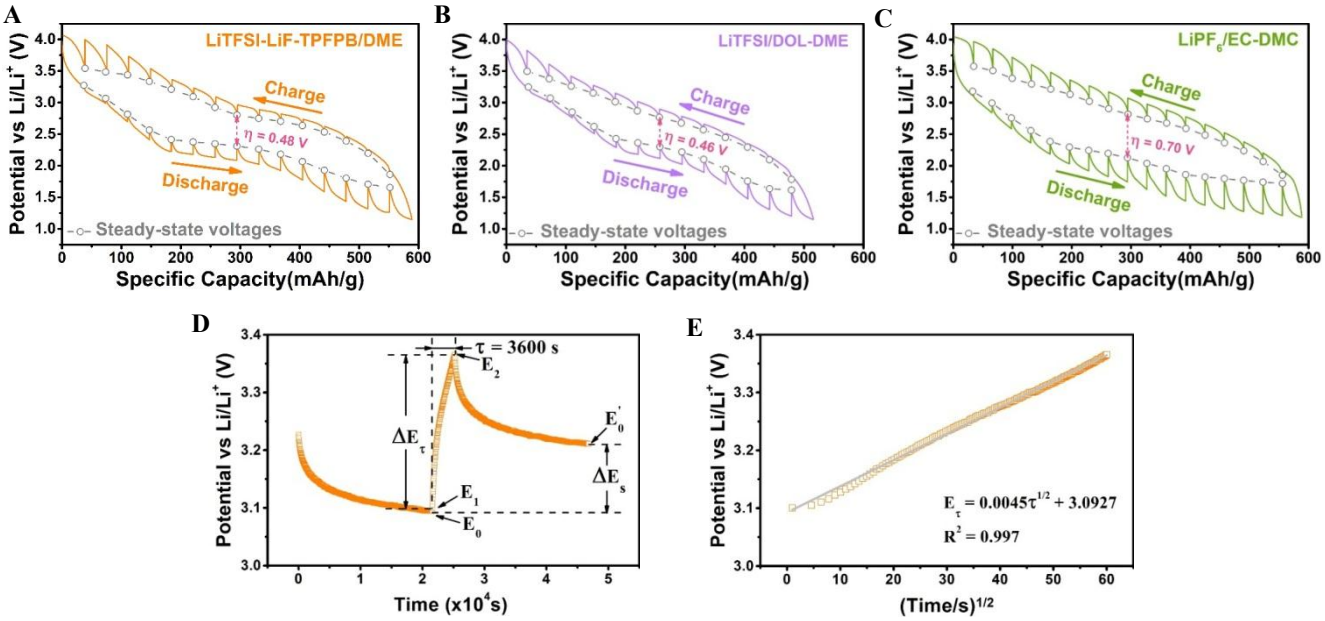

Figure S19. GITT measurement of $FeO_{0.3}F_{1.7}$ cathode in different electrolytes. GITT curves of $FeO_{0.3}F_{1.7}$ cathodes with the electrolytes of (**A**) LiTFSI-LiF-TPFPB/DME, (**B**) LiTFSI/DOL-DME and (**C**) $LiPF_6$/EC-DMC operated at a current density of 35 mA/g with an intermittent time of 1 h followed by an open-circuit relaxation for 6 h. (**D**) Voltage profiles of Li/$FeO_{0.3}F_{1.7}$ cell during a single GITT step in LiTFSI-LiF-TPFPB/DME electrolyte at ~3.23 V during charging. (**E**) Corresponding linear fitting of transient potential of cell (E_τ) as a function of square root of titration time ($\tau^{1/2}$).

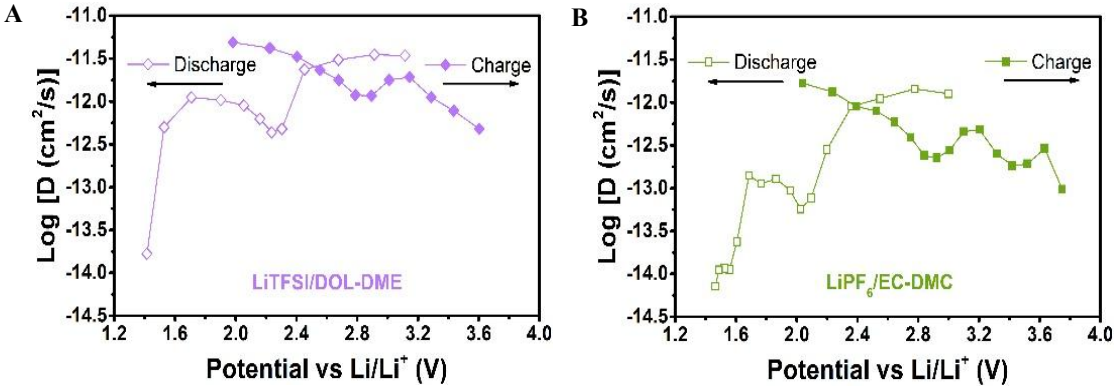

Figure S20. Kinetics performance of $FeO_{0.3}F_{1.7}$ cathodes in different electrolytes. Diffusion coefficient (D) plots of $FeO_{0.3}F_{1.7}$ cathodes in (**A**) LiTFSI/DOL-DME and (**B**) $LiPF_6$/EC-DMC electrolytes, as estimated by means of GITT measurement.

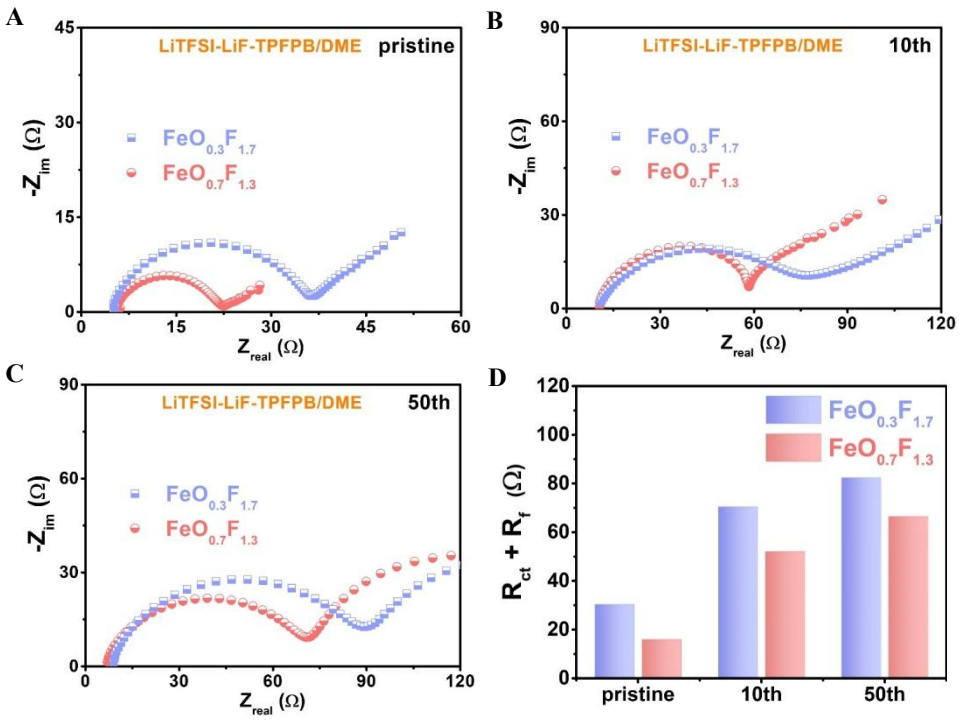

Figure S21. Electrochemical impedance spectra comparison of TPFPB-containing cells based on oxyfluoride cathodes with different O-contents. Nyquist plots of Li/$FeO_{0.3}F_{1.7}$ and Li/$FeO_{0.7}F_{1.3}$ cells (**A**) in pristine state, (**B**) after 10 cycles and after (**C**) 50 cycles at 100 mA/g. (**D**) Comparison of interface resistance R_i ($R_f + R_{ct}$) values for both the oxyfluoride cathodes at different cycling stages.

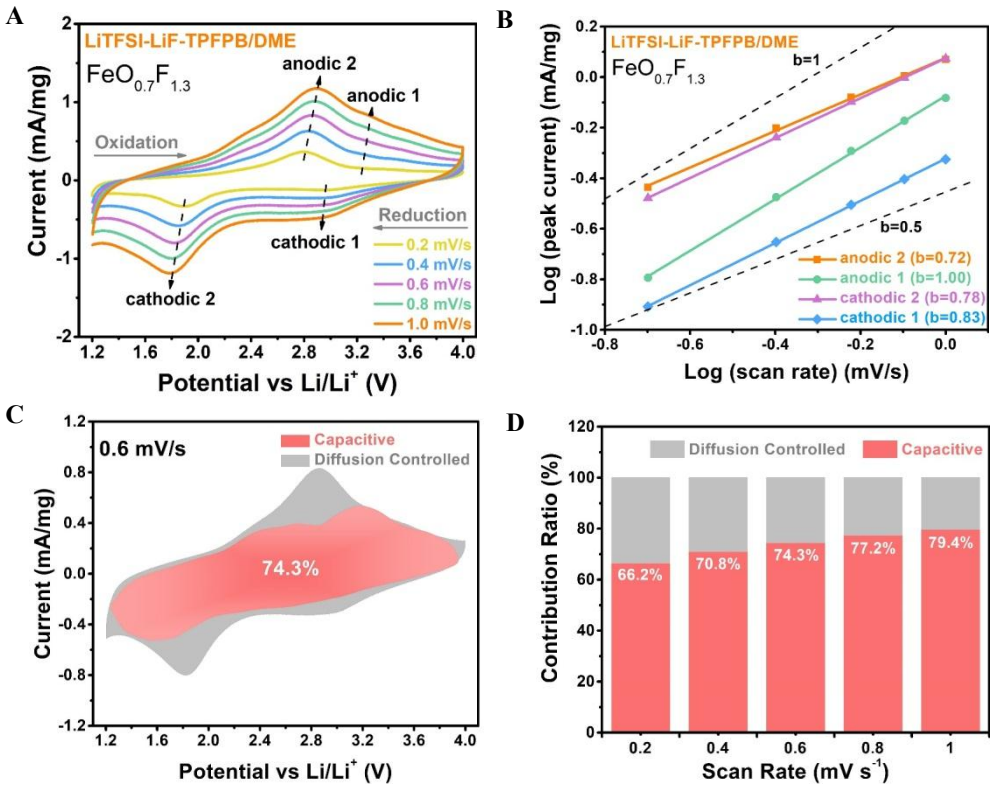

Figure S22. Quantitative analysis of charge-storage mechanism for $FeO_{0.7}F_{1.3}$ cathode using the electrolyte of LiTFSI-LiF-TPFPB/DME. (**A**) Typical CV profiles at various scan rates from 0.2 to 1.0 mV/s with the characteristic peaks labeled. (**B**) Power law dependence of measured current on scan rate at corresponding peak potentials. (**C**) Typical CV curve at 0.6 mV/s with divisional capacitive contribution (red area) and diffusion-controlled contribution (gray area). (**D**) Column graphs of scan-rate-dependent charge storage contributions from both capacitive and diffusion-controlled processes.

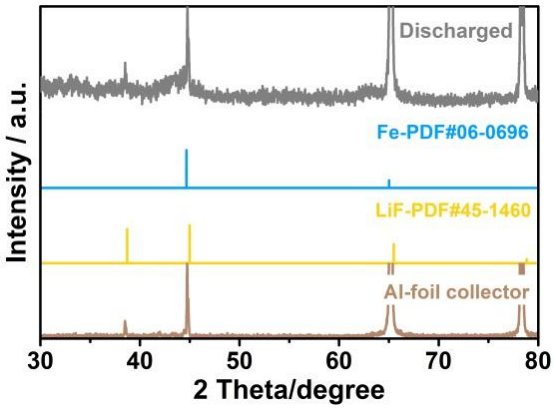

Figure S23. XRD pattern of cycled $FeO_{0.3}F_{1.7}$ cathode at discharged stage. The XRD investigation of discharged $FeO_{0.3}F_{1.7}$ cathode was performed after 5 cycles. The XRD pattern displays several sharp diffraction peaks, which mainly belong to the Al foil collector. Since these peaks are highly overlapped with the characteristic peaks of LiF and Fe, these conversion products cannot be accurately identified from the XRD result. The amorphization and electrochemical grinding of conversion products after several cycles would also influence the quality of diffraction peaks.

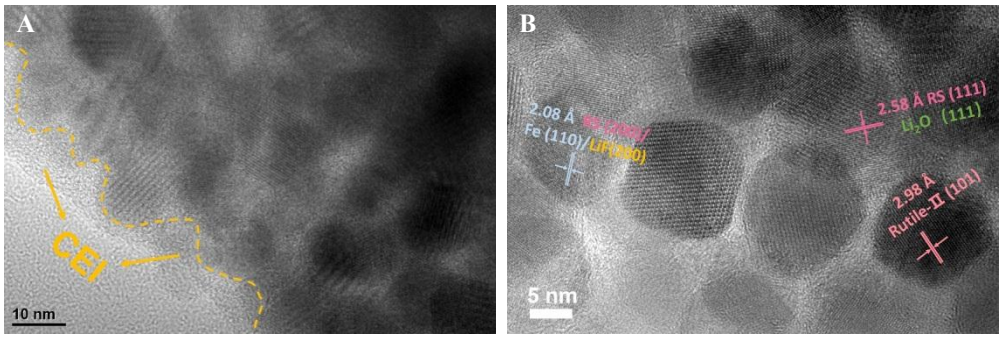

Figure S24. TEM measurement of lithiated $FeO_{0.3}F_{1.7}$ cathode. HRTEM images of $FeO_{0.3}F_{1.7}$ cathode after discharging to 1.2 V in LiTFSI-LiF-TPFPB/DME electrolyte at different regions with scale bars of (**A**) 10 nm and (**B**) 5 nm.

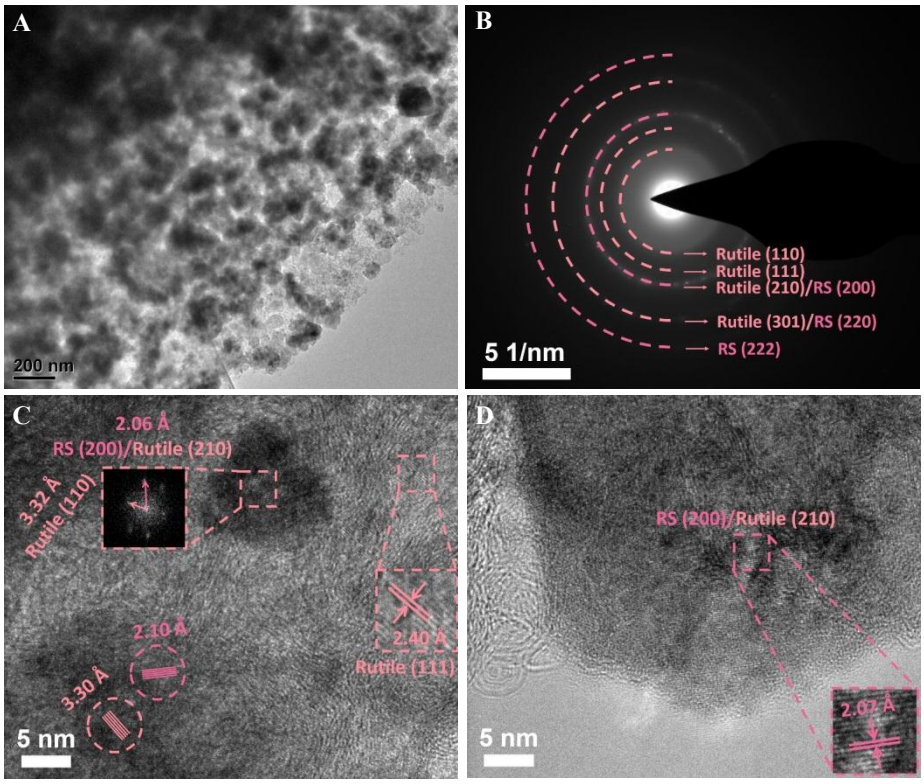

Figure S25. TEM measurement of delithiated $FeO_{0.3}F_{1.7}$ cathode. (**A**) TEM images of $FeO_{0.3}F_{1.7}$ cathode after charging to 4.0 V in LiTFSI-LiF-TPFPB/DME electrolyte and (**B**) corresponding SAED pattern with the diffraction rings assigned to rutile and rocksalt phases. (**C,D**) HRTEM images and FFT analysis in different amplified regions, indicating a tight contact between F-rich and O-rich phases.

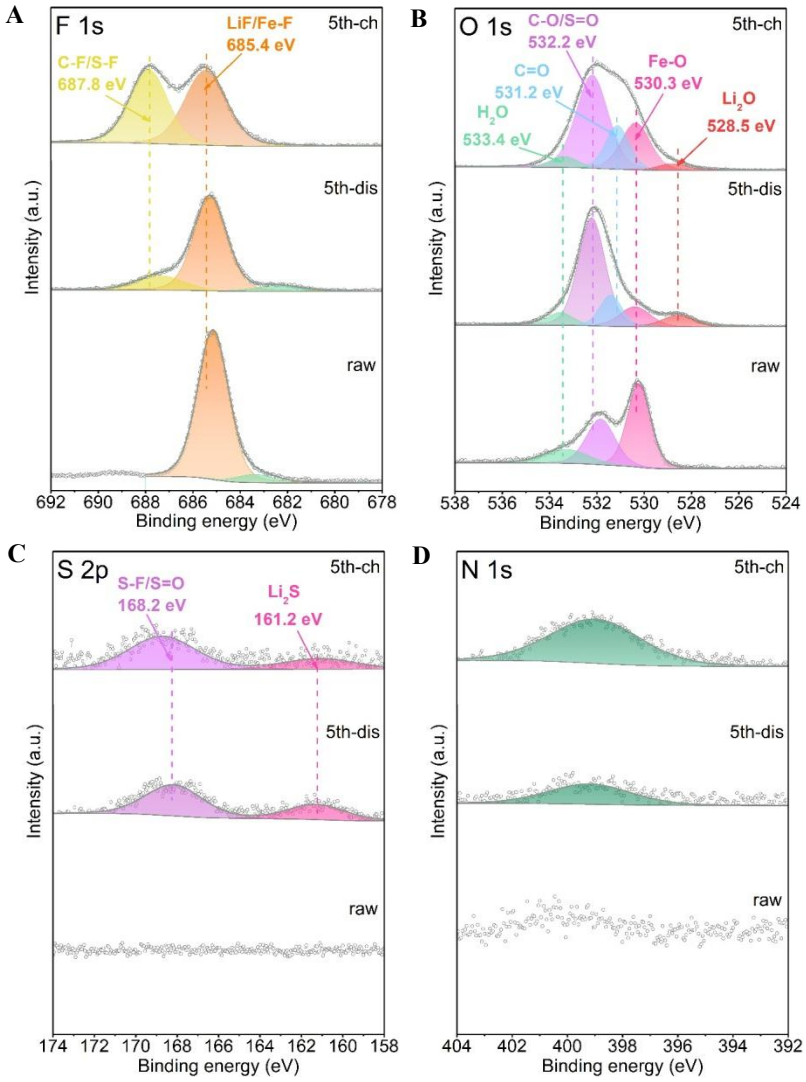

Figure S26. XPS analysis of cycled $FeO_{0.7}F_{1.3}$ electrodes in TPFPB-containing electrolyte. XPS spectra of (**A**) F 1s, (**B**) O 1s, (**C**) S 2p and (**D**) N 1s for pristine $FeO_{0.7}F_{1.3}$ electrode and cycled electrodes after discharging to 1.2 V and charging to 4.0 V. After discharging to 1.2 V, the peaks in Fe $2p_{3/2}$ shift to the positions of lower binding energies with the formation of rocksalt Li-Fe-O-F phase (at 709.9 eV), Li-Fe-F phase (at 712.9 eV) and Fe^0 (at 707.2 eV). According to the comparable binding energies of Li-Fe-O-F and Li-Fe^{2+}-O, a lower Fe oxidation state in rocksalt phase is indicated and is close to +2. The Fe $2p_{3/2}$ signal, belonging to the few undecomposed solid-solution Li-Fe-F phase, exhibits a reasonable binding energy value (712.9 eV) between those for Fe^{3+}-F (714.5 eV) and Fe^{2+}-F (711.5 eV). When recharging to 4.0 V, a regeneration of rutile peak and the positive displacement of rocksalt peak are observed with the concomitant dilution of metallic Fe peak in Fe $2p_{3/2}$ spectra.

For the high-spin Fe^{2+}/Fe^{3+}-species, the occurrence of shake-up satellite could be attributed to the excitation movement of valence electron from the 3d orbital into the empty 4s orbital by its interaction

with the emitted core 2p photoelectron. This shake-up process would reduce the kinetic energy of photoelectron, leading to a positive energy difference ΔE between satellite peak and its corresponding main peak ($\Delta E = E_{satellite\text{-}peak} - E_{main\text{-}peak}$). Iron cation with more unpaired valence electrons typically performs the enhanced shake-up process and consequently results in the increased ΔE value (e.g. ΔE values of 6.5 and 8.7 eV for Fe^{2+}-F and Fe^{3+}-F, respectively). In addition, the increase of ligand electronegativity can also induce the valence electron excitation of iron cation and enlarge the energy difference for satellite peak. (e.g. ΔE values of 5.9 and 6.5 eV for Fe^{2+}-O and Fe^{2+}-F, respectively). In addition, owing to the spin-orbit coupling interactions (e.g. between 2p core hole and unpaired 3d electron), the Fe 2p spectra for high-spin Fe^{3+}/Fe^{2+} species typically contain multiplet components within close space, leading to the broadened peak compared with that of Fe^0 metal.

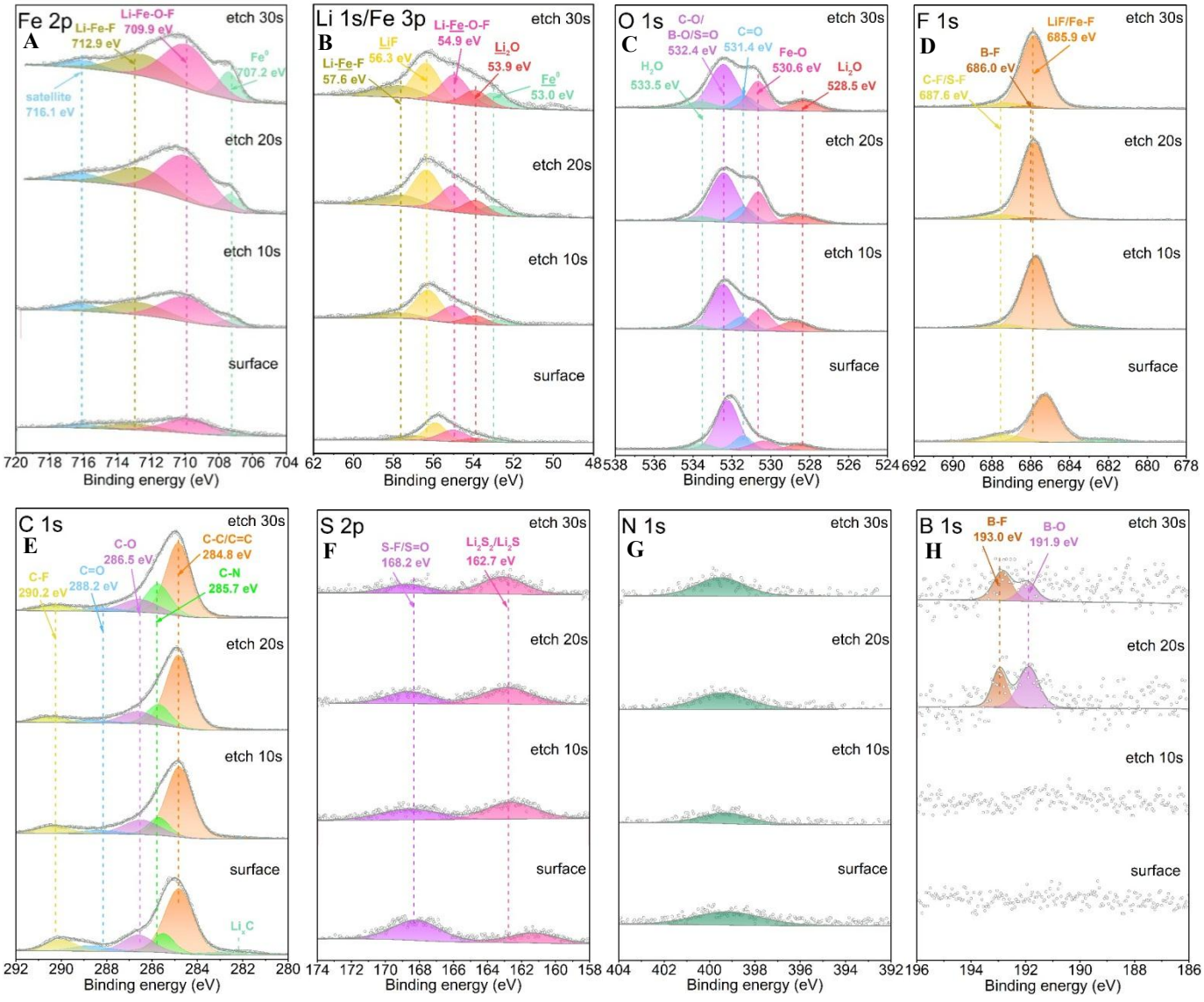

Figure S27. Depth analysis of surface chemical components for lithiated $FeO_{0.7}F_{1.3}$ electrode in TPFPB-containing electrolyte. XPS depth profiling spectra of (**A**) Fe $2p_{3/2}$, (**B**) Li 1s and Fe 3p, (**C**) O 1s, (**D**) F 1s, (**E**) C 1s, (**F**) S 2p, (**G**) N 1s and (**H**) B1s for lithiated $FeO_{0.7}F_{1.3}$ cathode after discharging to 1.2 V depending on different etching time.

Table S1. Determined molar concentration of each component for $FeO_{0.3}F_{1.7}$ and $FeO_{0.7}F_{1.3}$ samples from XRD Rietveld refinement result and their calculated theoretical specific capacities.

Sample	Composition	Molar percentage	Theoretical specific capacity
$FeO_{0.3}F_{1.7}$	$FeO_{0.32}F_{1.68}$	68.55%	673.42 mAh/g
	$FeF_3 \cdot 0.33H_2O$	31.45%	
$FeO_{0.7}F_{1.3}$	$FeO_{0.77}F_{1.23}$	85.51%	794.05 mAh/g
	FeF_3	14.49%	

Table S2. Computational detail of binding energy between TPFPB molecule and F atom. The energies of TPFPB molecule (E_{TPFPB}), F atom (E_F), TPFPB-F complex ($E_{TPFPB\text{-}F}$), and corresponding binding energy (E_b) are tabulated.

E_{TPFPB} (eV)	E_F (eV)	$E_{TPFPB\text{-}F}$ (eV)	E_b (eV)
-225.80	-0.09	-229.28	-3.39

Table S3. Computational data of the dissociation energies of LiF in the cases without and with anion acceptor TPFPB. The energies of LiF, Li atom, F atom, TPFPB molecule and TPFPB-F complex, and corresponding dissociation energies (E_d) are tabulated.

Cases	Initial state	Energy (kJ/mol)	Final state	Energy (kJ/mol)	E_d (kJ/mol)
LiF	LiF	-934.95	Li	-0.37	925.69
			F	-8.88	
LiF with TPFPB	LiF	-934.95	Li	-0.37	599.07
	TPFPB	-21787.38	TPFPB-F	-22122.88	

Table S4. Solubility comparison of LiF in DME without and with TPFPB based on the Li^+ concentration from ICP-OES measurement. The detection limit (DL) of Li for ICP-OES measurement is 0.004 μg/ml. The TPFPB concentration in LiF/DME solution is controlled at about 0.05 mol/l.

LiF/DME Solution	Li^+ concentration (mol/l)	Reaction molar ratio of TPFPB:LiF
Without TPFPB	< DL	-
With TPFPB	0.045	1:0.9

Table S5. Binding energies (eV) of Fe $2p_{3/2}$ spectra in different bonding situations for pristine $FeO_{0.3}F_{1.7}$/$FeO_{0.7}F_{1.3}$ samples and cycled $FeO_{0.7}F_{1.3}$ cathode according to the relevant references.

Bonding situation of Fe	Binding energy (eV) of Fe $2p_{3/2}$ spectra				Ref.
	Main peak		Satellite peak		
	This work	Ref.	This work	Ref.	
O-Fe^{3+}-F	711.6	711.5	717.8	-	[32]
Fe^{2+}-F	711.6	711.5	717.8	718.0	[33]
Fe^{3+}-F	714.3	714.5	Out of scope	723.2	[33]
Li-Fe-F	712.9	711.5 for Fe^{2+}-F 714.5 for Fe^{3+}-F	-	-	[33]
Li-Fe-O-F	709.9	709.3 for Li-Fe^{2+}-O	716.1	-	[62]
Fe^0	707.2	706.9	-	-	[63]